

# Numerical investigation of a Hall thruster plume: domain size, boundary conditions, cathode location

A. Domínguez-Vázquez,<sup>1, a)</sup> J. Zhou,<sup>2</sup> A. Sevillano-González,<sup>2</sup> and E. Ahedo<sup>2</sup>

<sup>1)</sup> Universidad de Málaga, 29071 Campanillas, Spain

<sup>2)</sup> Universidad Carlos III de Madrid, 28911 Leganés, Spain

(Dated: 16 March 2025)

The current-free expanding plasma beam from a Hall effect thruster with a lateral hollow cathode is investigated through a 2D axisymmetric hybrid particle-in-cell/fluid code. A new model imposing a global zero current condition at the plume downstream boundary is presented. This model outperforms the common local zero current condition, as it provides an estimation of the final potential of the plume and limits electron detachment from the magnetic lines induced by the plume boundary. Effects of plume size and cathode position on the plasma current solution in the plume and the coupling between cathode electrons and the ion beam are assessed for the two plume conditions. The new model provides a more robust current solution in the plume against plume truncation, especially when the externally-mounted cathode is outside the magnetic separatrix. This increases the reliability of the results for smaller, less computationally demanding plume domains, and is of central importance for validation of simulation results against experimental data from plume diagnostics. Compared to the operation with an externally-mounted cathode, positioned both inside and outside the magnetic separatrix, the discharge performance is enhanced for a centrally-mounted cathode due to the improved cathode-beam coupling, consistent with previous experimental and numerical studies.

## I. INTRODUCTION

In the near plume of a Hall effect thruster (HET) complex physical processes take place that remain not fully understood, and which play an important role in thruster performances and its integration with other spacecraft systems. Specifically, the neutralization of the expanding plasma jet and the interaction between the ion beam and the electron flow emitted from the neutralizer cathode are influenced by several factors, including the cathode's position<sup>1–6</sup>, its relative placement within the magnetic configuration<sup>7–10</sup>, and the electrical setup of the testing facilities<sup>11–14</sup>. Consequently, progress towards the development of an accurate and predictive model for the near plume of a HET is of significant importance.

Many hybrid particle-in-cell (PIC)/fluid<sup>15–21</sup> and multi-fluid<sup>22–24</sup> simulation models used in HET research typically simulate the plasma discharge inside the thruster channel and in a limited plume region. Simulating large plumes is computationally expensive and plume truncation is unavoidable. However, for a precise characterization of the discharge performance, simulations must include a sufficiently large portion of the plume. Effects of plume truncation on the numerical solution and, in particular, uncertainties on appropriate boundary conditions to be applied at the outflow boundary, hinder the validation of simulation models against experimental data from plasma diagnostics in the near plume. Therefore, setting appropriate boundary conditions at the downstream plume boundary of the finite simulation domain is of central importance. These must be consistent with the global neutralization of the electric

current in the far plume and the decay of the electric potential towards a uniform downstream value, representing either the infinity of free space or the metallic walls of a large vacuum chamber.

A widely adopted, although somewhat limiting, approach is the application of a local plume condition (LPC), which sets the plasma current to zero locally, i.e., at any point along the plume boundary<sup>17,20,22</sup>. While straightforward to implement, this assumption may only be valid for sufficiently large plumes and could introduce may lead to numerical errors if the truncated plume simulated is too small. For instance, Ref. 25 noted that H6 thruster multi-fluid simulations required to place the downstream boundary at a distance of at least 10 channel lengths downstream the thruster exit plane to avoid artificially increased electron transport across magnetic lines due to the zero local current condition. Moreover, the LPC model gives no information about the final potential in the plume nor the electron energy flux through the plume boundary. Previous numerical studies with multi-fluid<sup>22,26</sup> and hybrid<sup>17,27</sup> models set the electron temperature at the plume boundary. In Ref. 26 it is found that the temperature solution in the near field (from about three channel lengths downstream the thruster exit) is largely driven by the prescribed boundary value, which is informed from plasma measurements. Therefore, to be consistent, this approach requires accurate electron temperature measurements in the plume, which may be only available for a limited range of operational conditions.

The first goal of this paper is to present a global plume condition (GPC) model, which enforces a net current-free condition at the plume boundary, while locally decoupling ion and electron currents there. Unlike the LPC model, the GPC model allows for the estimation of the final potential of the plume at infinity and provides an expression for the electron energy flux at the plume bound-

---

<sup>a)</sup> Electronic mail: [adoming@uma.es](mailto:adoming@uma.es)

ary. The second, complementary goal here is to evaluate the robustness of the plasma solution in the near plume region with respect to plume size for both the GPC and LPC models. For that purpose, four different plume sizes will be considered.

Finally, the third goal of this paper is to analyze the influence of the cathode position on the neutralization of the ion beam current emitted by the thruster through the electron flow emitted from the cathode, as well as the coupling voltage required for this process. In the near plume of HET with a conventional (i.e., non-shielded) magnetic topology, an off-axis magnetic separatrix (MS) surface typically exists, which separates closed and open magnetic field lines. Several experimental studies have shown a significant impact on performance and plasma variables when the externally-mounted (i.e., off-axis) cathode is positioned either inside or outside the MS<sup>7–10</sup>. These two cases will be analyzed here. The magnetic field line passing through the center of the cathode injection surface will be referred to as the cathode magnetic line (CML), and it guides the trajectory of the central portion of the emitted magnetized electron beam. When the cathode is placed inside the MS, the CML forms a closed loop within the near plume. In contrast, when the cathode is positioned outside the MS, the CML extends farther downstream and intersects the boundary of the truncated plume. In this case, the plasma behavior in the plume is expected to be more influenced by the size and boundary of the plume. On the other hand, other experimental<sup>2,4</sup> and numerical<sup>28,29</sup> studies have compared the operation with externally and centrally-mounted (i.e., on-axis) cathodes, and have reported lower plume divergence and higher efficiency when the cathode was located at the axis. Here, we will also investigate the operation with a centrally-mounted cathode.

All analyses in this paper will be based on numerical simulations of a 5kW-class HET with a lateral hollow cathode, conducted using the axisymmetric hybrid (particle/fluid) code HYPHEN<sup>20,30,31</sup>.

The rest of the paper is organized as follows. Sec. II presents the GPC model and its implementation within HYPHEN. Sec. III compares the simulation results obtained with both the GPC and LPC models for four plume sizes, with the cathode placed inside the MS. Sec. IV presents the results for both the GPC and LPC models and two plume sizes when the cathode is positioned outside the MS. Finally, Sec. V summarizes the conclusions.

## II. SIMULATION DETAILS

### A. Setup and model

A 5 kW-class HET similar to a PPS5000<sup>32,33</sup>, with a conventional (non-shielded) magnetic topology and a hollow cathode is considered for this study. Figs. 1(b)–(c) sketch the simulation domain, which comprises the

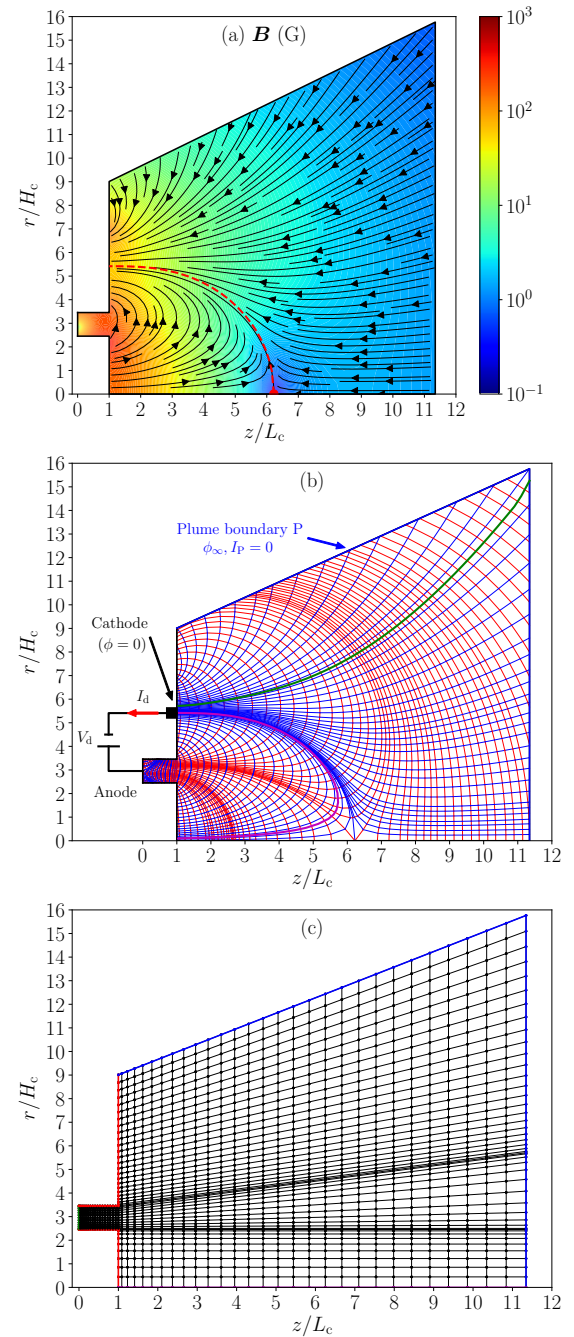


FIG. 1. (a) 2D ( $z, r$ ) contour map and streamlines of  $\mathbf{B}$ . The dashed red line corresponds to the MS, and the red circle marker indicates the magnetic singular point. (b) The MFAM used by the E-module. Inner blue and red lines are  $B$ -parallel and  $B$ -perpendicular lines, respectively, defining the cells. The magenta and green lines correspond to the CML for cathodes 1 and 2, respectively. (c) The PIC mesh used by the I-module. The red, green and magenta lines indicate the thruster dielectric walls, the anode wall and the symmetry axis, respectively. All figures correspond to plume size P3.

thruster annular vessel (with length  $L_c = 29$  mm, width  $H_c = 22.2$  mm and inner radius 54.5 mm), and a near-

1 plume region of different sizes. Fig. 1(a) shows the applied magnetic field  $\mathbf{B}$  magnitude map and streamlines. The peak of  $B \equiv |\mathbf{B}|$  along the thruster channel midline is 196.05 G, at  $z/L_c = 0.86$ . The dashed red line in Fig. 1(a) indicates the (off-axis) MS in the near plume, which passes through the magnetic singular point located at the axis at  $z/L_c = 6.2$ . The magnetic lines are represented by the blue lines in Fig. 1(b). Downstream of the MS, the magnetic topology exhibits a magnetic nozzle (MN) shape, which will channel the plasma beam in the far plume<sup>34</sup>.

2 The thruster anode covers the complete channel back wall and the cathode, located at the thruster exit plane, can be either externally-mounted (i.e., off-axis), as depicted in Fig. 1(b), or centrally-mounted (i.e., at the axis). A power source sets a discharge voltage  $V_d = 300$  V between anode and cathode. The reference of the electric potential  $\phi$  is set at the cathode, so that the potential of the anode wall is  $V_d$ . The thruster operates with xenon and the total neutral mass flow rate injected into the domain is  $\dot{m} = \dot{m}_A + \dot{m}_C$ , where  $\dot{m}_A = 17.59$  mg/s and  $\dot{m}_C = 1.32$  mg/s are the flow rates injected through the anode and the cathode, respectively (details on neutral injection conditions can be found in Ref. 20). The discharge current  $I_d$  collected at the anode wall provides the electron flow injected at the cathode. The temperature of the electrons emitted from the cathode is set to 2.25 eV.

3 The plasma discharge is simulated with the axisymmetric hybrid code HYPHEN, whose characteristics have been detailed in previous works<sup>20,30,35,36</sup> and are briefly outlined next. The code is composed of three main modules coupled within a time-marching sequential loop. The ion (I)-module operates on a structured mesh of the simulation domain, shown in Fig. 1(c), and implements a particle-in-cell (PIC) method to solve the dynamics of the heavy species (i.e., ions and neutrals, including singly and doubly charged ions; charge exchange collisions (CEX) generating slow ions and fast neutrals in the plume are also considered) obtaining the net ion density  $n_i$  and ion current density vector  $\mathbf{j}_i$ .

4 The electron (E)-module solves a quasineutral drift-diffusion fluid model for the magnetized electron population on an unstructured magnetic field align mesh (MFAM)<sup>37</sup>, obtained from  $\mathbf{B}$  and shown in Fig. 1(b), where red lines correspond to magnetic equipotential lines. Setting the plasma density  $n_e = n_i$ , it provides the solution for the electric potential  $\phi$ , the electron temperature  $T_e$ , the electron current density vector  $\mathbf{j}_e$  (and thus the electric current density vector  $\mathbf{j} = \mathbf{j}_e + \mathbf{j}_i$ ), and the energy flux vector  $\mathbf{P}_e'' = 5n_e T_e \mathbf{u}_e / 2 + \mathbf{q}_e$  (sum of enthalpy and heat fluxes). Interpolation between the PIC mesh and the MFAM is required to transfer plasma properties. The axisymmetric electron fluid model needs to be completed with empirical submodels for electron-wall interaction properties and for the turbulent cross-field transport due to high-frequency electron instabilities. As in Ref. 20, here we set a turbulent electron collisionality

5 of the form  $\alpha_t(z)\omega_{ce}$ , with  $\omega_{ce} = eB/m_e$  the electron cyclotron frequency and  $\alpha_t(z)$  a “step-out” type tuning function representing the local electron turbulence level, which features two calibration parameters  $\alpha_{t1} = 1.2\%$  and  $\alpha_{t2} = 4.8\%$ , fitted to reproduce PPS5000 the experimental values for  $I_d$  and thrust ( $F$ ) at the operating point under consideration. The transition point from  $\alpha_{t1}$  to  $\alpha_{t2}$  is located downstream the B peak, at  $z/L_c = 1.49$ .

6 Non-neutral effects are limited to thin, planar Debye sheaths, which are treated as electrostatic discontinuities around the thruster walls, and solved by the sheath (S)-module. This provides the appropriate boundary conditions for the wall-collected electron current density  $j_{ne} = \mathbf{1}_n \cdot \mathbf{j}_e$  and energy flux  $P_{ne}'' = \mathbf{1}_n \cdot \mathbf{P}_e''$  at each (quasineutral) MFAM boundary face, with  $\mathbf{1}_n$  being the outward unit normal vector. The local sheath potential fall is also determined. The sheath model includes secondary electron emission at dielectric walls, and retains non-Maxwellian features of the electron velocity distribution function (VDF), such as the replenishment fraction of the VDF tail corresponding to impacting electrons<sup>38</sup>, which is set here to a 30%. Further details on the model parameters and implementation for dielectric and conducting walls (e.g. the anode wall at known potential  $V_d$ ) can be found in Ref. 20.

## B. Simulation cases

7 Four different plume domains (P1 to P4) are considered, featuring plume axial extensions of 100, 200, 300 and 400 mm ( $3.4L_c$ ,  $6.9L_c$ ,  $10.3L_c$  and  $13.8L_c$ ). For all cases, the plume domain extends radially up to 200 mm at the thruster exit plane (see Fig. 1). The radial extension of the downstream end increases with the plume length and is set to 250, 300, 350 and 400 mm for P1 to P4 cases, respectively, so that the PIC mesh adapts to the ion beam expansion in the plume to limit particle depletion. As an example, Figs. 1(b) and (c) show the MFAM and the PIC mesh for domain P3, respectively. The main characteristics of the simulation domain meshes for cases P1 to P4 and the simulation timestep are listed in Tab. I.

8 As outlined in Sec. I, three distinct cathode configurations are considered: cathode 1 (C1) and cathode 2 (C2) correspond to an externally-mounted cathode positioned inside and outside the MS at radial distances of 120 mm and 126.6 mm, respectively, while cathode 3 (C3) represents a centrally-mounted cathode aligned with the thruster axis. The magenta and green lines in Fig. 1(b) represent the corresponding closed and open CML for C1 and C2, with the latter intersecting the downstream axial boundary below the top right corner of the plume domain. For C3 the CML coincides with the symmetry axis. For plume size P1 and cathode C1, the axial downstream boundary of the plume intersects the closed CML and the magnetic singular point is left outside the plume domain.

Simulation parameter	Units	Value
I-module mesh smallest grid size	mm	1
I-module mesh number of cells	-	969, 1284, 1509, 1734
I-module mesh number of nodes	-	1049, 1371, 1601, 2831
MFAM number of cells	-	1948, 2397, 3506, 4081
MFAM number of faces	-	4025, 4933, 7186, 8353
MFAM average cells skewness	$(10^{-2})$	7.06, 6.45, 5.49, 5.31
Ion-moving timestep, $\Delta t$	ns	15

TABLE I. Main simulation parameters and mesh characteristics (values separated by commas correspond to plume sizes P1 to P4).

### C. Conditions at the plume boundary

Consider the case where the plasma beam from the HET expands into free space (or into a large vacuum chamber with low background pressure). The blue line in Fig. 1(b) represents the boundary P of the simulated plume. Boundary conditions must be defined at each point on P, ensuring they are “compatible” with the expected plasma behavior between P and infinity. It is assumed that the plasma beam is current-free, and that the electric potential decreases monotonically to a value  $\phi_\infty$  at infinity (with respect to the cathode). This implies that: first, the current-free condition applies at P as well; and second, ions exiting the simulated plume domain will ultimately reach infinity, while individual electrons leaving P may either reach infinity or be reflected back into the simulation domain. The electron fluid model, as used in HYPHEN, must be consistent with this behavior.

As discussed in Sec. I, the conventional approach is to apply a local plume condition (LPC), which replaces the global zero-current condition with the more restrictive, yet simpler to implement, condition of zero local current, that is

$$j_{neP} = -j_{niP}, \quad (1)$$

at any point of the boundary P. In addition, the electron energy flux is set to

$$P''_{neP} = -cT_{eP}j_{neP}/e, \quad (2)$$

where the positive constant  $c$  is set empirically.

Previous HYPHEN simulations for a magnetically shielded HET reported in Ref. 20 used  $c = 9/2$ . Other studies have set  $T_{eP}$ , instead of  $P''_{neP}$ , in both multi-fluid<sup>22,26</sup> and hybrid<sup>17,27</sup> HET simulations. The 2D hybrid HET simulations in Ref. 39 applied a Neumann boundary condition,  $dT_e/d\mathbf{1}_n = 0$  at P, which is equivalent to  $q_{neP} = 0$ , thus yielding  $c = 5/2$ . Multi-fluid simulations of a magnetic nozzle have shown that electron cooling is highly sensitive to the type of boundary condition (i.e., Dirichlet or Neumann) applied to  $T_{eP}$ <sup>40</sup>. HYPHEN simulations of an electrodeless plasma thruster in Ref. 36 used  $c = 5/2, 9/2$  and  $13/2$ , revealing a significant impact of  $c$  on the electron temperature, with

$c = 9/2$  providing the best agreement for two plume domain sizes. Here, we set  $c = 9/2$  when the LPC is applied.

As an alternative to the LPC, we propose here a global plume condition (GPC) which imposes the global zero current condition at P as

$$I_P = I_{eP} + I_{iP} = \int_P [j_{ne}(\phi_{\infty P}) + j_{ni}] dS = 0, \quad (3)$$

where: the surface integral is performed over P;  $I_{eP}$  and  $I_{iP}$  are the outwards electron and ion currents at P, respectively;  $j_{niP}$  is provided by the I-module at any point of P; and, assuming a Maxwellian VDF for electrons,  $j_{neP}(\phi_{\infty P})$  is

$$j_{neP}(\phi_{\infty P}) = -en_{eP}\sqrt{\frac{T_{eP}}{2\pi m_e}} \exp\left(\frac{-e\phi_{\infty P}}{T_{eP}}\right), \quad (4)$$

at any point of P, with  $\phi_{\infty P} = \phi_P - \phi_\infty$ . Eq. (3) is an implicit equation for  $\phi_\infty$ , which is solved iteratively [by linearizing Eq. (4)]. Once  $\phi_\infty$  is known, the boundary condition  $j_{neP}$  at any point of P is known from Eq. (4).

With respect to the electron energy flux, we assume at infinity the expression

$$P''_{ne\infty} = -2T_{eP}j_{neP}/e, \quad (5)$$

based again on a Maxwellian electron VDF. Then the boundary condition at P for the energy flux is

$$P''_{neP} = P''_{ne\infty} - j_{neP}\phi_{\infty P} = -j_{neP}\frac{T_{eP}}{e}\left(2 + \frac{e\phi_{\infty P}}{T_{eP}}\right). \quad (6)$$

Notice that the sum between parentheses would correspond here to the arbitrary constant  $c$  in Eq. (2).

### III. INFLUENCE OF PLUME SIZE AND BOUNDARY CONDITIONS

Solutions for plume sizes P1 to P4 with C1, and using the GPC and LPC, are compared here. The eight simulation cases will be denoted as GP*i*C1 and LP*i*C1 ( $i = 1, 2, 3, 4$ ), corresponding to the GPC and LPC, respectively. We begin with the maps of electron plasma currents, as these are the most significantly affected. This is followed by the maps of scalar plasma variables, and finally, the performance results.

Fig. 2 plots the in-plane electric current density  $\tilde{\mathbf{j}} = \mathbf{j} - j_\theta \mathbf{1}_\theta$  for the eight cases. All of them satisfy  $I_P = 0$ . The boundary condition at P affects mainly the  $\tilde{\mathbf{j}}$  solution downstream of the CML. In this region, the LPC forces all current loops to close within the plume domain. Therefore, current loops outward of the CML are clearly different for different plume sizes. In contrast, with the GPC, current loops change much less with the plume size since they are not constrained to close within the plume domain (the electric current at P can be locally

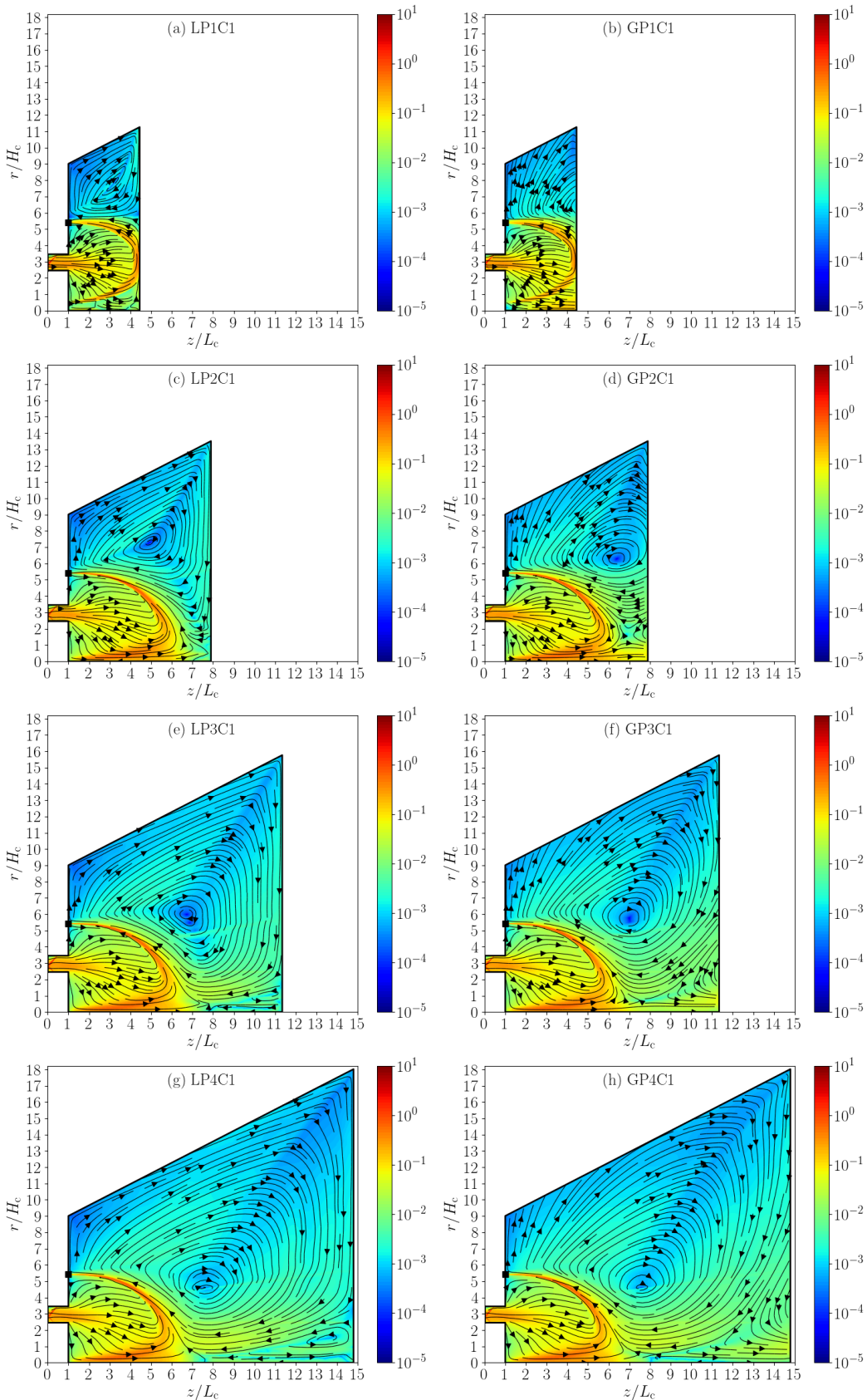


FIG. 2. Plume sizes P1-P4 with cathode 1 (black square marker) and with LPC (left column) and GPC (right column). 2D  $(z,r)$  contour maps and streamlines of  $\hat{j}$  ( $\text{Acm}^{-2}$ ).

nonzero), which makes GPC much more robust against plume truncation and more physically plausible.

Focusing now on the region inwards the CML, similar anode-to-cathode current loops are found for cases P2 to P4, but not for P1, where part of the CML has been left outside the plume. This indicates that P1 is not a good choice for the simulations: when the cathode is placed inside the MS, the domain must include integrally the closed CML. Nonetheless, the case GP1C1 outperforms LP1C1 since its  $\tilde{\mathbf{j}}$  solution remains much closer to that of the P2-P4 cases.

For the eight simulation cases the solution for the in-plane ion current density,  $\tilde{\mathbf{j}}_i = \mathbf{j}_i - j_{\theta i} \mathbf{1}_\theta$ , is practically identical, and exhibits the characteristic ion divergence of a HET plume; it is shown in Fig. 3(a) for size P3. This near identity of behavior is due to the fact that  $\phi$  variations among cases in the downstream part of the plume (shown later) are much smaller than  $V_d$  (or the average ion energy in that region), so that the ion flow is practically unaffected. Note that downstream of the MS, where the magnetic topology features a MN shape, the near-unmagnetized ions detach inwardly from the magnetic lines, as expected<sup>41</sup>.

Differences on  $\tilde{\mathbf{j}}$  among cases are thus due quasi exclusively to  $\tilde{\mathbf{j}}_e$ . Figs. 3(b) and (c) show this current for cases GP3C1 and LP3C1, respectively. For the two cases, the center of the electron beam travels along the CML. The component of this beam closest to the MS diffuses towards it and then exits outwards, primarily near the magnetic singular point, to neutralize the ion beam. The main differences among cases are found in the outwards flow of electrons, especially in the lateral part of the plume. The LPC in case LP3C1 promotes electron detachment from the magnetic lines, yielding a higher electron current towards the lateral plume boundary to locally cancel the ion current there (mainly carried by high-divergence fast ions and slow CEX ions generated in the core of the plasma beam exiting the thruster channel). This result is in line with the simulations reported in Ref. 25, where the authors note that if the plume boundaries are set too close to the channel exit, the transport of electrons in the near plume gets perturbed by the zero local current condition, and more electron current across magnetic field lines may occur. Electron detachment near the plume boundary has also been observed in HYPHEN simulations of an electrodeless plasma thruster with a MN, where the LPC was used<sup>36</sup>. In contrast, in case GP3C1, the electron current towards the lateral plume boundary is lower, and the electron streamlines follow more closely the local magnetic field lines, exhibiting a more progressive outward detachment towards the lateral boundary. This solution is more representative of the still well-magnetized electron population in the simulated plume region: the surface-averaged values over P of  $B$  and the effective Hall parameter, for plume sizes P1 to P4, decrease from 7.4 to 1.8 G, and from 212.2 to 68.1 G, respectively.

Fig. 4 compares main plasma variables at the plume

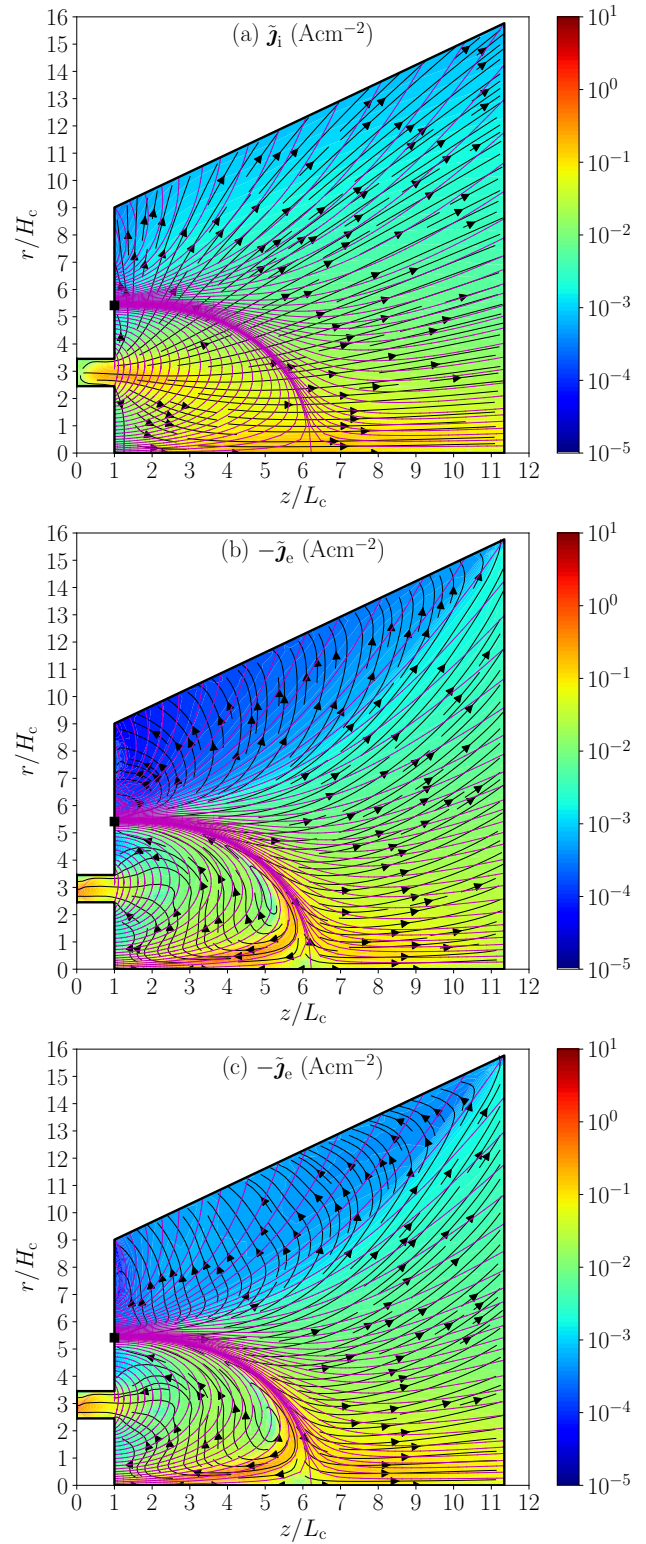


FIG. 3. 2D ( $z, r$ ) contour maps of (a)  $\tilde{\mathbf{j}}_i$  and (b)  $\tilde{\mathbf{j}}_e$  for case GP3C1, and (c)  $\tilde{\mathbf{j}}_e$  for case LP3C1. The black lines with arrows depict streamlines of  $\tilde{\mathbf{j}}_i$  in (a) and  $-\tilde{\mathbf{j}}_e$  in (b) and (c). Magenta lines indicate magnetic lines. The black square marker indicates the location of cathode 1.

boundary P for all cases with plume size P3. The spatial variable runs from the axis to the upper-right corner and continues on the lateral boundary. We focus now on the results for C1 cases. Fig. 4(a) quantifies the differences in electron currents commented above. The ion current is the practically same for both GP3C1 and LP3C1. Conversely, while the electron current is set equal to the ion current in case LP3C1, in case GP3C1, there is an electron current deficit along the lateral plume boundary, which is compensated by an increased electron current along the axial plume boundary.

Fig. 4(b) compares the profiles of the electric potential at P. The main differences are observed at the lateral plume boundary, resulting from the different electron current collected there: higher  $\phi_P$  values relative to the cathode are required in case LP3C1 in order to extract a larger electron current, which is constrained to match the ion current locally by the LPC. Fig. 4(c) compares the electron temperature at P, showing non-negligible differences and lower values for GP3C1 along most of the plume boundary. Fig. 4(d) shows the average energy deposited by exiting electron  $\mathcal{E}_{neP} = -eP_{neP}''/j_{neP}$  and the average energy per unit of outward ion current at P  $\mathcal{E}_{niP} = eP_{niP}''/j_{niP}$ . An added value of the GPC is that  $\mathcal{E}_{neP}$  is computed from Eq. (6) yielding values ranging from  $4.0T_{eP}$  to  $9.2T_{eP}$  for case GP3C1, whereas the LPC sets it “arbitrarily” to  $4.5T_{eP}$ . According to Eq. (6), this implies that  $e\phi_{\infty P}/T_{eP} \approx 2.0\text{-}7.2$  for case GP3C1.

Fig. 5 shows the axial profiles of plasma scalar variables along the channel midline for  $z/L_c \geq 3$ ; for  $z/L_c < 3$  (not shown), all cases present very similar profiles for all variables, with peak values  $T_e \approx 28$  eV and  $n_e \approx 1.7 \cdot 10^{18} \text{ m}^{-3}$ . We focus now on the profiles for C1 cases. Despite the significant changes across different cases on plasma variables in the lateral part of the plume commented above (especially in the plasma current maps), there is consistency on these profiles for the different plume sizes and boundary conditions. Although the maximum difference in electric potential within the plume, observed for case LP1C1, is only about 2% of  $V_d$ , it is of the same order as the local electron temperature and is therefore significant for diagnostics in the near plume.

Tab. II lists the main performance figures for the eight simulation cases, beginning with the cathode coupling voltage,  $V_{cc}$ . For plume size P1,  $V_{cc}$  values correspond to the electric potential at the plume boundary at the channel midradius. For plume sizes P2-P4,  $V_{cc}$  is estimated as the electric potential value at the crossing point between the channel midline and the CML<sup>42</sup>, showing maximum differences of around 1% of  $V_d$ . This indicates a very similar effective ion acceleration in the discharge for all cases, which is in line with the very small differences (below 2%) observed in the thrust,  $F$ , among cases, as listed in Tab. II. The values of  $F_e$ ,  $F_i$ , and  $F_n$  correspond to the contributions to thrust (i.e., the downstream axial momentum fluxes) from the electron, ion, and neutral species, including CEX populations. As expected, elec-

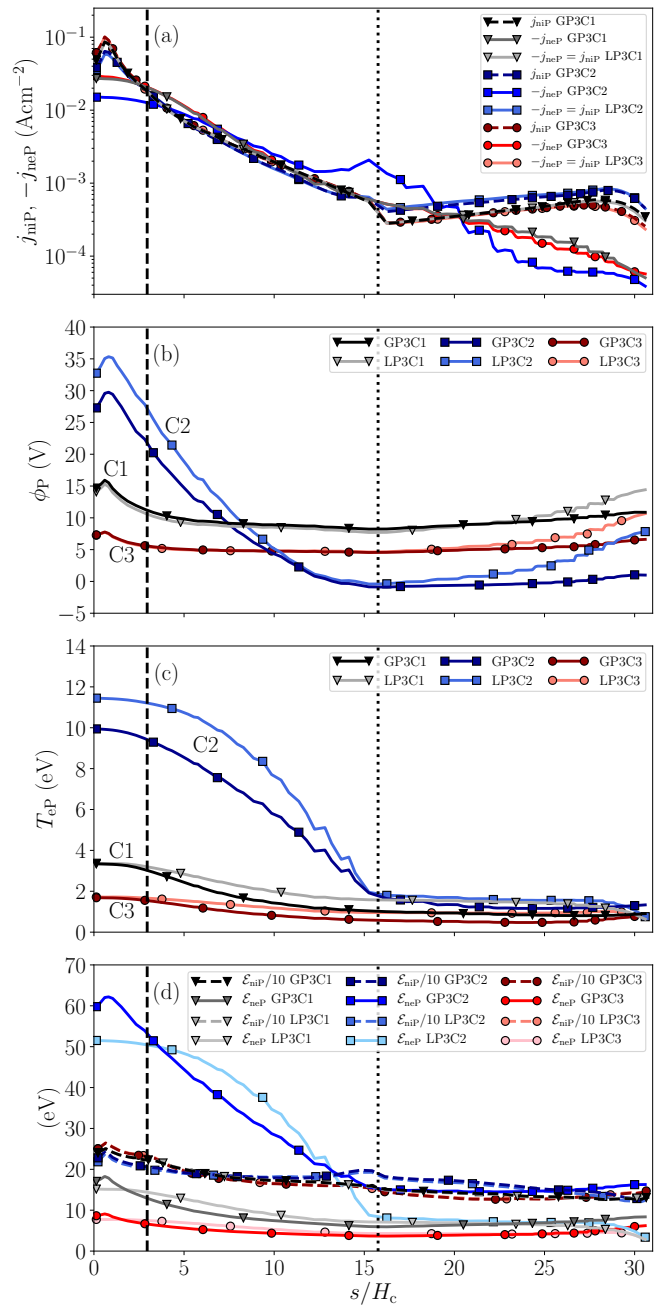


FIG. 4. Plume size P3. Comparison of profiles along P for the GPC and LPC. (a)  $j_{niP}$  and  $-j_{neP}$ , (b)  $\phi_P$ , (c)  $T_{eP}$  and (d)  $\mathcal{E}_{neP}''$  and  $\mathcal{E}_{niP}''/10$ . Coordinate  $s$  runs along P with  $s = 0$  at the symmetry axis. The vertical black dashed and dotted lines correspond to the thruster channel midradius and the upper-right corner of the plume domain, respectively.

tron momentum flux is transferred to ion momentum flux as the plasma beam moves downstream. The small increase (on average) in thrust with the plume size is due to the small magnetic force over the plasma there. It is assumed that the residual magnetic force between P and infinity has no relevant impact in thrust.

An important asset of the GPC is the determination

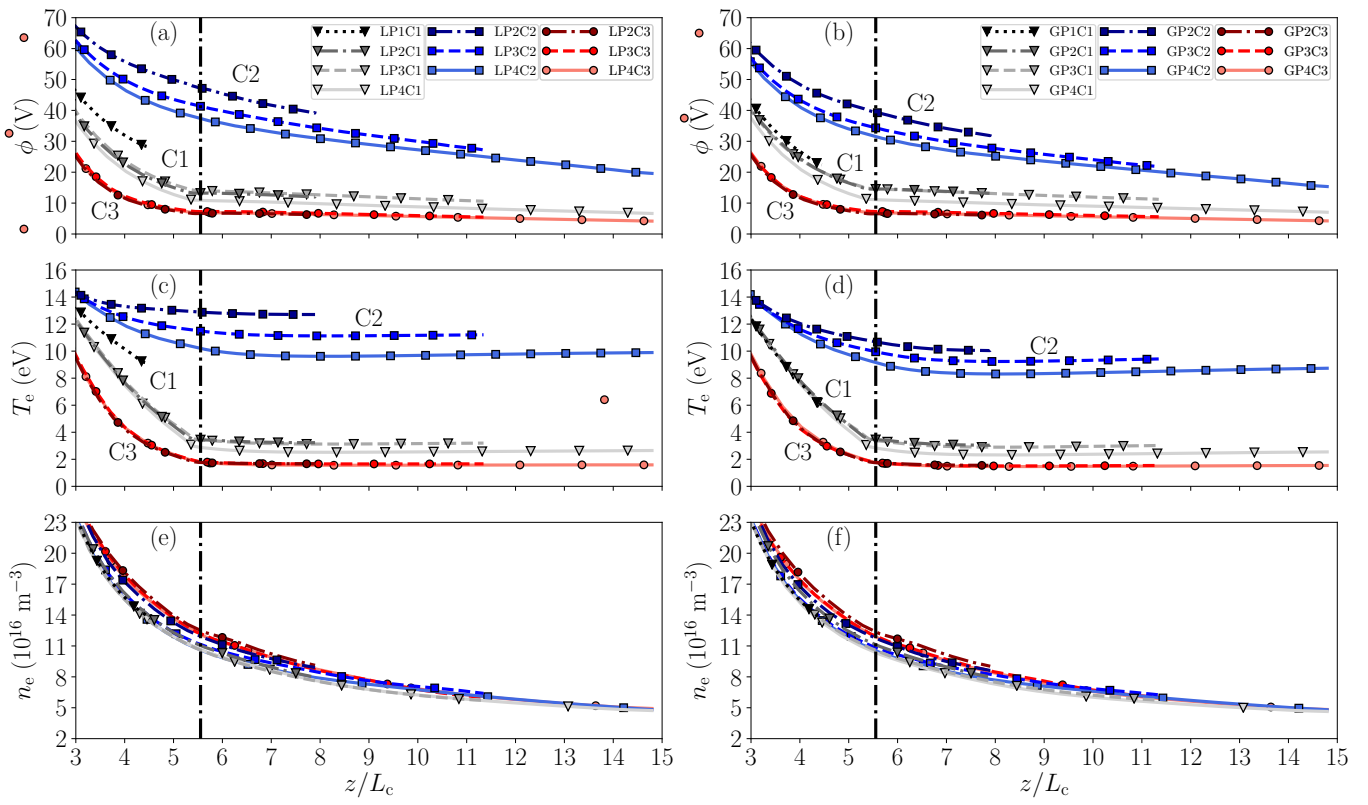


FIG. 5. 1D axial profiles along the thruster channel midline in the near-plume region for cases with the LPC (left column) and the GPC (right column). The vertical black dot-dashed line indicates the crossing point with the MS at  $z/L_c = 5.6$ .

of the potential at infinity,  $\phi_\infty$ , also given in Tab. II for the four plume sizes. For sufficiently large plumes, i.e., plume sizes P2-P4,  $\phi_\infty$  monotonically decreases with the plume size, as expected. The total decrease from P2 to P4 amounts to about 78% of its value for P2: 30% from P2 to P3 and 48% from P3 to P4. This suggests that simulating a plume size larger than P4 would be necessary for a more precise estimation of  $\phi_\infty$ . However, the results indicate that increasing the plume size leads to only incremental variations in  $\phi$  along the thruster channel midline and  $F$ , and thus the effect on discharge performance is minimal. Moreover, the quality of the MFAM tends to deteriorate significantly for very large plumes.

The ion beam current through P,  $I_{iP}$ , (equal to the electron one in absolute value in all cases) is practically the same for all cases, with maximum differences of about 2%, as listed in Tab. II. For plume size P3, around a 14% of it is collected at the lateral plume boundary, which is the fraction of  $I_{eP}$  collected there for case LP3C1. For case GP3C1, this fraction decreases to 10%, consistent with the lower electron current at the lateral plume boundary shown in Fig. 4(a).

The plasma power balance is detailed in the Appendix A and shows only small variations (below 2%) in its different contributions across cases. As shown in Tab. II, differences in  $I_d$  are also very small (around 1% maxi-

	GP1C1	GP2C1	GP3C1	GP4C1	LP1C1	LP2C1	LP3C1	LP4C1
$V_{cc}$ (V)	22.38	14.57	14.75	11.20	28.34	13.22	14.15	10.97
$\phi_\infty$ (V)	5.80	6.17	4.31	1.33	N/A	N/A	N/A	N/A
$F$ (mN)	280.1	284.0	283.9	286.5	279.6	286.0	284.8	286.1
$F_i$ (mN)	274.7	280.6	281.1	284.4	272.3	282.3	281.9	284.0
$F_e$ (mN)	4.3	2.4	1.7	1.0	6.3	2.8	1.9	1.0
$F_n$ (mN)	1.1	1.0	1.1	1.1	1.0	1.0	1.0	1.1
$I_{iP}$ (A)	16.29	16.68	16.72	16.72	16.40	16.69	16.67	16.63
$I_d$ (A)	17.75	17.91	17.74	17.85	17.81	17.98	17.86	17.82
$P$ (kW)	5.46	5.39	5.34	5.35	5.34	5.41	5.37	5.34
$\eta$	0.39	0.40	0.40	0.41	0.39	0.40	0.40	0.41
$\eta_{ene}$	0.65	0.64	0.65	0.65	0.65	0.64	0.64	0.65
$\eta_{div}$	0.77	0.78	0.79	0.77	0.77	0.78	0.78	0.78
$\eta_{disp}$	0.78	0.80	0.78	0.81	0.78	0.80	0.80	0.80

TABLE II. Performance figures for plume sizes P1 to P4 with C1 and the GPC and LPC.

mum), and therefore also in power  $P \approx V_d I_d \approx 5.4$  kW and thrust efficiency  $\eta = F^2/(2\dot{m}P) \approx 40\%$ . According to Eq. (A.2),  $\eta$  is conveniently factored as the product of three partial efficiencies, which are defined in Eq. (A.3): the energy efficiency,  $\eta_{ene}$ , which represents the fraction of the total power deposited into P; the divergence efficiency,  $\eta_{div}$ ; and the dispersion efficiency,  $\eta_{disp}$ . The latter two partial efficiencies are plume-related metrics that assess plume divergence and velocity dispersion, respectively. These partial efficiencies also show slight

1 changes (maximum 3%) between cases. (Note that we  
 2 aim to highlight here that the differences between cases  
 3 are minimal and not the values themselves.)

4 Therefore, for a cathode located inside or at the MS,  
 5 and provided that the size of the simulated plume region  
 6 is sufficiently large such that  $\phi$  variations in the down-  
 7 stream part of the plume are much smaller than  $V_d$ , we  
 8 conclude that thruster performance is well determined  
 9 regardless of whether the LPC or GPC is used. Nonethe-  
 10 less, it is evident that plume size and conditions signif-  
 11 icantly impact plasma current maps within the plume,  
 12 which is important for plume characterization and com-  
 13 parison with experimental data (noting that the plume  
 14 is the plasma region most accessible to diagnostics).

15 Finally, Figs. 5(c) and (d) reveal that for sizes P2-  
 16 P4,  $T_e$  remains nearly constant at relatively low values,  
 17 around 2.5 eV, downstream the MS, and no significant  
 18 electron cooling is observed, in line with the results in  
 19 Ref. 26. Previous kinetic studies on magnetized plumes  
 20 have shown that the total potential fall to infinity in the  
 21 plume is primarily determined by the electron thermal  
 22 energy<sup>43</sup>. Here, the surface-averaged value of  $e\phi_{\infty P}/T_{eP}$   
 23 over P varies slightly with plume size, ranging between  
 24 4.7 and 5.7 (which, taking  $T_{iP}/T_{eP} \approx 10$ , as obtained  
 25 here, agrees very well with simulations for a magnetic  
 26 nozzle in Ref. 43). Since  $T_{eP} \sim 1\text{eV}$ ,  $\phi_{\infty P}$  still amounts  
 27 to about 15-20% of the potential drop in the near plume  
 28 downstream of  $z/L_c = 3$ . Increasing plume size results  
 29 in only a small decrease in  $\phi_P$  and the Hall parameter,  
 30 but not in  $T_{eP}$ . This suggests that anomalous parallel-  
 31 field electron cooling<sup>44</sup> should be considered in the MN  
 32 region of the plume, similar to the approach taken for  
 33 electrodeless plasma thruster simulations with HYPHEN  
 34 in Ref. 36.

#### 35 IV. EFFECTS OF CATHODE LOCATION ON CURRENT 36 MAPS AND CATHODE COUPLING

37 This section presents an analysis of the results for  
 38 plume sizes P2 to P4 with C2 (i.e., an externally-mounted  
 39 cathode positioned outside the MS) and C3 (i.e., a  
 40 centrally-mounted cathode aligned with the thruster  
 41 axis), considering both the GPC and LPC. The cor-  
 42 responding simulation cases will be referred to as GP*i*C<sub>j</sub>  
 43 and LP*i*C<sub>j</sub> ( $i = 2, 3, 4$ ;  $j = 2, 3$ ) for the GPC and LPC,  
 44 respectively.

45 Tab. III lists the main performance figures for C2  
 46 cases.  $V_{cc}$  values correspond to the electric potential at  
 47 the plume boundary at the channel midradius, and ex-  
 48 hibit a monotonic decrease with the plume size for both  
 49 GPC and LPC cases. As for C1 cases, the thrust  $F$  in-  
 50 creases with the plume size for both GPC and LPC cases  
 51 due to the residual magnetic force on the plasma. For  
 52 GPC cases,  $\phi_{\infty}$  is negative and decreases with the plume  
 53 size. Compared to C1 cases (refer to Tab. II), C2 cases  
 54 show a higher variability with the plume size of the val-  
 55 ues of  $V_{cc}$ ,  $F$  and  $\phi_{\infty}$  for GPC cases, which suggests that

56 simulating larger plume sizes is required when the cath-  
 57 ode is placed outside the MS.

58 Tab. IV gathers the main performance figures for C3  
 59 cases.  $V_{cc}$  is estimated as the electric potential at the  
 60 crossing point between the channel midline and the MS.  
 61 Contrary to C2 cases,  $V_{cc}$  does not follow a clear trend  
 62 with plume size, and the maximum variations among  
 63 cases are lower than for C1 cases, amounting to just 0.3%  
 64 of  $V_d$ . Consistent with this result, differences in  $F$  across  
 65 C3 cases are also smaller (approximately 0.8% maximum)  
 66 than those in C1 cases. For GPC cases,  $\phi_{\infty}$  values are  
 67 positive, as in C1 cases, and follow a monotonically de-  
 68 creasing trend with plume size. However,  $\phi_{\infty}$  varies less  
 69 with plume size, with a total decrease from P2 to P4  
 70 amounting to approximately 72% of its P2 value: 21%  
 71 from P2 to P3 and 51% from P3 to P4.

72 Similar to C1 cases, the ion beam current through P,  
 73  $I_{iP}$ , exhibits low variations with plume size for both C2  
 74 and C3 cases. For plume sizes P2-P4, the average value  
 75 of  $I_{iP}$  is 16.66A for C1 and C2 cases, and 17.15A for  
 76 C3 cases. For plume size P3 and cathode C2 and C3,  
 77 around a 20% and 13% of  $I_{iP}$ , respectively, is collected  
 78 at the lateral plume boundary (for C1 it is around a 14%).  
 79 While for LPC cases it coincides with the fraction of  $I_{eP}$   
 80 collected there, for GPC cases, however, this fraction de-  
 81 creases to about 13% and 9% (it is about 10% for C1).  
 82 Fig. 4(a) shows the electron current density profiles at P  
 83 for GP3C1, GP3C2 and GP3C3. Compared to GP3C1,  
 84 GP3C3 exhibits a lower electron current in the lateral  
 85 part of the plume. In contrast, case GP3C2 shows a lo-  
 86 cal maximum of  $-j_{neP}$  near the upper-right corner of the  
 87 plume domain, along with locally higher electron current  
 88 values in the lateral plume boundary nearby.

89 As in C1 cases, the impact of the plume size and the  
 90 plume condition (i.e., GPC or LPC) on  $I_d$  is also very  
 91 small for C2 and C3 cases, and thus on power and thrust  
 92 efficiency. Compared to C1 cases, the average value of  
 93  $I_d$  and thus of  $P \simeq V_d I_d$  is about 3% lower for C2 cases  
 94 and 2% higher for C3 cases. However, while C2 cases  
 95 exhibit lower  $\eta$  values than C1, C3 cases show higher  
 96 values, with changes in  $\eta$  of approximately 2–3% across  
 97 cases. Therefore, the lower (higher)  $\eta$  in C2 (C3) cases  
 98 is attributed to the corresponding decrease (increase) in  
 99  $F$ . For C2 cases lower  $F$  values result from the decrease  
 100 in the ion contribution to thrust,  $F_i$ , which is not com-  
 101 pensated by the increase in the electron contribution,  $F_e$ .  
 102 The weaker cathode-beam coupling indicated by the in-  
 103 crease in  $V_{cc}$ , which rises from approximately 4–5% of  $V_d$   
 104 for C1 cases (refer to Tab. II) to values ranging from  
 105 5% to 13% of  $V_d$ , correlates with the observed reduction  
 106 in  $F_i$ . The opposite behavior is observed for C3 cases:  
 107  $F_e$  becomes marginal (even lower than the contribution  
 108 from fast neutrals from CEX), and the higher  $F_i$  leads  
 109 to an overall increase in  $F$ . This trend aligns with the  
 110 lower  $V_{cc}$ , indicating improved coupling between cathode  
 111 electrons and the ion beam exiting the thruster channel.

111 Compared to C1 cases, partial efficiencies results for  
 112 C2 cases reveal (we report changes in absolute terms) a

	GP2C2	GP3C2	GP4C2	LP2C2	LP3C2	LP4C2
$V_{cc}$ (V)	32.28	21.76	15.36	39.68	27.18	19.61
$\phi_\infty$ (V)	-4.95	-12.75	-14.78	N/A	N/A	N/A
$F$ (mN)	271.4	272.1	275.2	268.0	269.4	274.4
$F_i$ (mN)	264.5	267.1	271.7	259.6	263.4	270.4
$F_e$ (mN)	6.0	4.1	2.6	7.5	5.1	3.1
$F_n$ (mN)	0.9	0.9	0.9	0.9	0.9	0.9
$I_{iP}$ (A)	16.49	16.61	16.54	16.62	16.79	16.66
$I_d$ (A)	17.24	17.20	17.34	17.15	17.17	17.27
$P$ (kW)	5.18	5.31	5.20	5.14	5.15	5.18
$\eta$	0.37	0.37	0.38	0.37	0.37	0.38
$\eta_{ene}$	0.70	0.69	0.71	0.69	0.69	0.70
$\eta_{div}$	0.71	0.70	0.71	0.71	0.70	0.71
$\eta_{disp}$	0.75	0.76	0.76	0.76	0.77	0.77

TABLE III. Performance figures for plume sizes P2 to P4 for C2 cases with GPC and LPC.

decrease of 6–9% in  $\eta_{div}$  and 2–5% in  $\eta_{disp}$ , indicating higher plume divergence and velocity dispersion, respectively, which is not compensated by the 4–6% increase in  $\eta_{ene}$ . In contrast, C3 cases exhibit the opposite behavior, with lower plume divergence and velocity dispersion:  $\eta_{div}$  increases by 1–3% and  $\eta_{disp}$  by 2–4%, while  $\eta_{ene}$  remains unchanged or decreases by just 1%.

Several experimental and numerical studies have reported results consistent with the behavior of  $V_{cc}$ ,  $F$ ,  $\eta$ , and plume divergence observed here. For an externally-mounted cathode, Ref. 1 reported a decrease in thrust with increasing radial position of the cathode, leading to the conclusion that the optimal cathode position is as close as possible to the outer magnet pole. Various experimental works have reported an increase in  $V_{cc}$  and poorer performance when increasing the radial position of the externally-mounted cathode, in particular for locations outside the MS<sup>7–10</sup>. Measurements on a HET with an externally-mounted cathode and a magnetic topology lacking an off-axis separatrix indicated that  $V_{cc}$  increased in magnitude with the radial position of the cathode when the cathode was moved across regions of high electron magnetization, where the effective Hall parameter was about 500<sup>12</sup>. Here, the effective Hall parameter in the cathode region is of about 215, 350 and 52 for C1, C2 and C3 cases, respectively.

For a 6 kW HET, Jameson *et al.*<sup>2</sup> compared the performance with externally and centrally-mounted (i.e., on-axis) cathodes. Higher  $V_{cc}$  values were observed when operating with the externally-mounted cathode, while efficiency was reported to increase by 2–3% when using the centrally-mounted cathode. Compared to the operation with an externally-mounted cathode, reduced  $V_{cc}$  and plume divergence were also reported in Ref. 4 for a 8 kW HET with a centrally-mounted cathode. Full PIC 2D axial-radial simulations<sup>28,29</sup> have captured the lower plume divergence found in experiments when operating with a centrally-mounted cathode.

	GP2C3	GP3C3	GP4C3	LP2C3	LP3C3	LP4C3
$V_{cc}$ (V)	6.53	7.36	6.92	6.63	7.32	6.94
$\phi_\infty$ (V)	2.65	2.10	0.74	N/A	N/A	N/A
$F$ (mN)	297.1	294.9	296.6	296.7	296.2	298.6
$F_i$ (mN)	294.1	292.3	294.3	293.4	293.5	296.3
$F_e$ (mN)	1.6	1.1	0.7	1.9	1.2	0.7
$F_n$ (mN)	1.4	1.5	1.6	1.4	1.5	1.6
$I_{iP}$ (A)	17.19	17.19	17.08	17.18	17.16	17.07
$I_d$ (A)	18.34	18.13	18.19	18.38	18.24	18.20
$P$ (kW)	5.56	5.50	5.52	5.57	5.53	5.52
$\eta$	0.42	0.42	0.42	0.42	0.42	0.43
$\eta_{ene}$	0.64	0.64	0.64	0.63	0.63	0.64
$\eta_{div}$	0.80	0.80	0.79	0.80	0.81	0.81
$\eta_{disp}$	0.82	0.82	0.84	0.83	0.82	0.83

TABLE IV. Performance figures for plume sizes P2 to P4 for C3 cases with GPC and LPC.

As shown in Fig. 5, C2 cases exhibit higher values of  $\phi$  and  $T_e$  along the channel midline than C1 cases. The plasma density also increases slightly along the channel midline and decreases near the axis (not shown), yielding similar average values in the plume ranging from  $2.1 \cdot 10^{16} \text{ m}^{-3}$  to  $4.0 \cdot 10^{16} \text{ m}^{-3}$ , and decreasing with plume size. For plume size P3, Fig. 4(b) shows higher  $\phi$  values near the axis and the midradius along the axial plume boundary, and lower values along the lateral plume boundary. This results in a higher radial electric field in the plume (not shown), which is the primary responsible for the higher plume divergence and velocity dispersion of C2 cases. Fig. 4(c) shows higher  $T_e$  values, especially along the axial plume boundary. A similar result is observed in Fig. 4(d) for the average electron energy at P,  $\mathcal{E}_{neP}$ . The increase in  $\eta_{ene}$  of C2 cases, compared to C1 cases, is due to the larger power deposited into P by hotter electrons, while the ion power at P decreases due to their lower acceleration. Compared to case GP3C1, for case GP3C2 the total electron power at P,  $P_{eP}$  is about 4.4 times higher, while the total ion power at P,  $P_{iP}$  is just 3.1% lower ( $P_{eP}$  and  $P_{iP}$  are obtained as the surface integral over P of  $P''_{niP} = \mathcal{E}_{niP} j_{niP}/e$  and  $P''_{neP} = -\mathcal{E}_{neP} j_{neP}/e$ , respectively).

In contrast, Fig. 5 reveals that C3 cases exhibit lower values of  $\phi$  and  $T_e$  along the channel midline than C1 cases. On the other hand,  $n_e$  is larger along the channel midline and the axis (not shown), yielding higher average values in the plume ranging from  $2.5 \cdot 10^{16} \text{ m}^{-3}$  to  $4.4 \cdot 10^{16} \text{ m}^{-3}$ , and decreasing with plume size. For plume size P3, Fig. 4(b) shows lower and more uniform  $\phi$  values at P, consistent with the lower plume divergence and velocity dispersion of C3 cases. Similarly, Figs. 4(c) and (d) depict lower and more uniform  $T_e$  and  $\mathcal{E}_{neP}$  values at P.

The trends with the cathode location found here for  $\phi$ ,  $T_e$ , and  $n_e$  in the near plume are well aligned with previous experimental works. Measurements in Ref. 3 for an externally-mounted cathode indicated that operating

the thruster from a more distant cathode rather than a closer one yields higher plasma potential and electron temperature, as well as lower plasma density in the near plume. Sommerville *et al.*<sup>7</sup> showed that average values of  $\phi$  and  $T_e$  in the near plume increase with the radial position of the externally-mounted cathode, particularly outside the MS, while average  $n_e$  values remained practically unchanged or decreased slightly. The authors noticed that higher  $\phi$  values led to larger ion beam divergence due to the enhanced radial electric field. Plasma potential in the plume was also reported to increase when the externally-mounted cathode was placed outside the MS in Refs. 8 and 9, with the latter study reporting higher divergence. Compared to the operation with a centrally-mounted cathode, higher plasma potential in the plume was also observed for a 6 kW HET<sup>2</sup> when operating with an externally-mounted cathode.

Compared to C1 cases, the surface-averaged values of  $e\phi_{\infty P}/T_{eP}$  over P are slightly lower for C3 cases ranging between 4.3 and 4.8 (with  $T_{iP}/T_{eP} \approx 15-20$ ). The average value of  $T_{eP}$  is of about 0.7 eV, and the potential drop from P to infinity amounts to about 15% of the potential drop in the near plume downstream of  $z/L_c = 3$ . In contrast, C2 cases exhibit higher surface-averaged values of  $e\phi_{\infty P}/T_{eP}$ , ranging from 5.7 to 6.7, and lower values of  $T_{iP}/T_{eP} \approx 5$ . The trend of  $e\phi_{\infty P}/T_{eP}$  with  $T_{iP}/T_{eP}$  found here is consistent with the simulation results for a MN reported in Ref. 43. The higher electron temperature in the plume for C2 cases, with average value of  $T_{eP}$  of about 3 eV increases the potential drop between P and infinity for these cases, which amounts to about 32% of the potential drop in the near plume downstream of  $z/L_c = 3$ , reaching up to 6% of  $V_d$ . The lack of a model for the anomalous cooling of magnetized electrons in the MN part of the near plume emerges as a more notable limitation in this scenario.

Figs. 6(a)-(d) show  $\tilde{\mathbf{j}}$  for C2 cases with plume sizes P3 and P4. As discussed in Secs. II B and III, for plume sizes P2-P4 and C1, the CML is enclosed by the MS (blue dashed line in Fig. 6), forming a closed loop within the simulated plume domain, which is located sufficiently far from the P boundary. Therefore, in these cases, the plume is already globally current-free downstream of the CML, although not locally, since the anode-to-cathode current loop is closed within the MS. In contrast, for C2 cases, the CML (red dashed line in Fig. 6) extends downstream along the plume and intersects the P boundary. The anode-to-cathode current loop closes downstream of the MS, below the CML, and a second counter-rotating current loop forms above the CML. When the LPC is applied, current streamlines of these two counter-rotating current loops are constrained to be parallel to the P boundary, so that they must necessarily converge at a plasma stagnation point at P featuring  $\tilde{\mathbf{j}} = 0$ . Therefore, the current solution provided by the LPC is inherently dependent on the plume size: observe in Figs. 6(a) and (c) how, for cases LP3C2 and LP4C2, this point moves with the downstream boundary of the plume, and the

electric current loops in the near plume exhibit notable differences in the region common to both cases. On the other hand, by locally decoupling ion and electron currents at P, the GPC allows these current loops to close *at infinity*. As a result, the influence of the P boundary on the current solution is significantly reduced, making it much more robust to variations in plume size. In particular, the plasma stagnation point at P, which is induced artificially by the LPC, is absent when the GPC is applied. Instead, a  $\tilde{\mathbf{j}} = 0$  point appears within the domain, located at a similar position for both P3 and P4 sizes.

Figs. 6(e)-(h) show  $\tilde{\mathbf{j}}_e$  for the same cases above (as for C1 cases, differences on  $\tilde{\mathbf{j}}$  are primarily due to  $\tilde{\mathbf{j}}_e$ ; the ion current shows minor differences among cases and has been omitted in the figure). The central part of the electron beam emitted by cathode C2 travels downstream along the CML and, for case GP3C2, gives rise to the local maximum of  $-j_{nep}$  shown in Fig. 4(a) near the upper-right corner of the plume domain, where the CML intersects the P boundary. Note the magnetic separation of these electrons, similar to that of C1 cases. Now, only the fraction of electrons emitted by the cathode closest to the MS travels along it towards the singular point, where they penetrate into the interior region of the separatrix and subsequently into the thruster channel. This behavior has also been observed in three-dimensional hybrid simulations of the near plume of a HET with a similar magnetic topology, when the external cathode is placed in the lateral region of the plume, outside the MS<sup>21</sup>.

Finally, Fig. 7 shows  $\tilde{\mathbf{j}}$  and  $\tilde{\mathbf{j}}_e$  maps for C3 cases with plume sizes P3 and P4. The solution for  $\tilde{\mathbf{j}}$  and  $\tilde{\mathbf{j}}_e$  downstream of the MS is similar to that found for C1 cases, as described in Sec. III. The main differences compared to C1 cases arise in the anode-to-cathode current loop inside the MS: the centrally-mounted cathode generates significantly higher local  $\tilde{\mathbf{j}}$  and  $\tilde{\mathbf{j}}_e$  in the cathode near-plume along the axis and enhances the coupling between cathode electrons and the ion beam exiting the thruster channel. This improvement occurs because the outermost component of the electron beam emitted from the cathode diffuses towards the thruster exit plane well upstream of the MS, prior to reaching it.

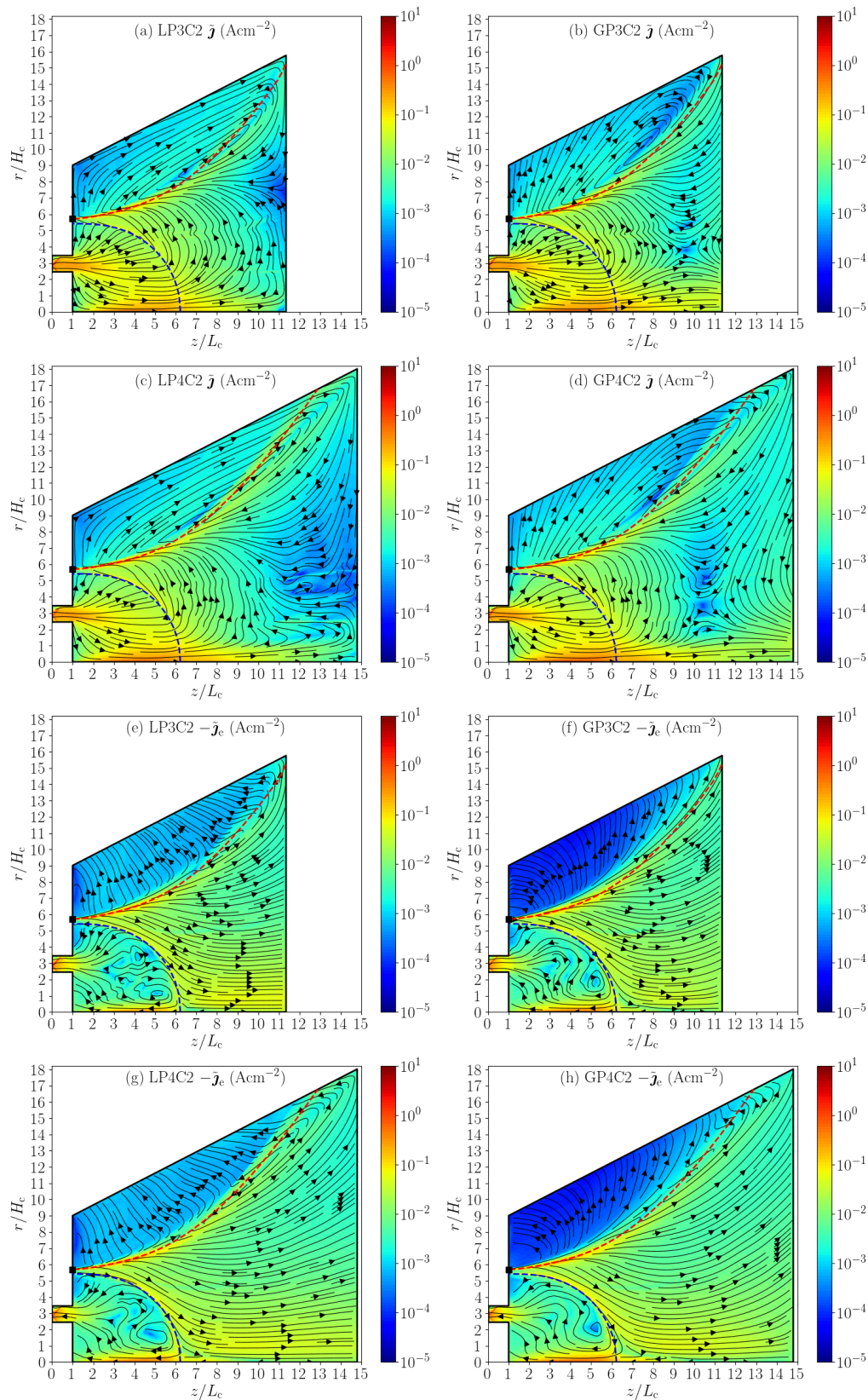


FIG. 6. Plume sizes P3 and P4 with C2 (black square marker) and with LPC (left column) and GPC (right column). 2D ( $z, r$ ) contour maps of  $\bar{j}$  (a)-(d) and  $-\bar{j}_e$  (e)-(h). The black lines with arrows depict streamlines of  $\bar{j}$  and  $-\bar{j}_e$ . The red and blue dashed lines correspond to the CML and the MS, respectively.

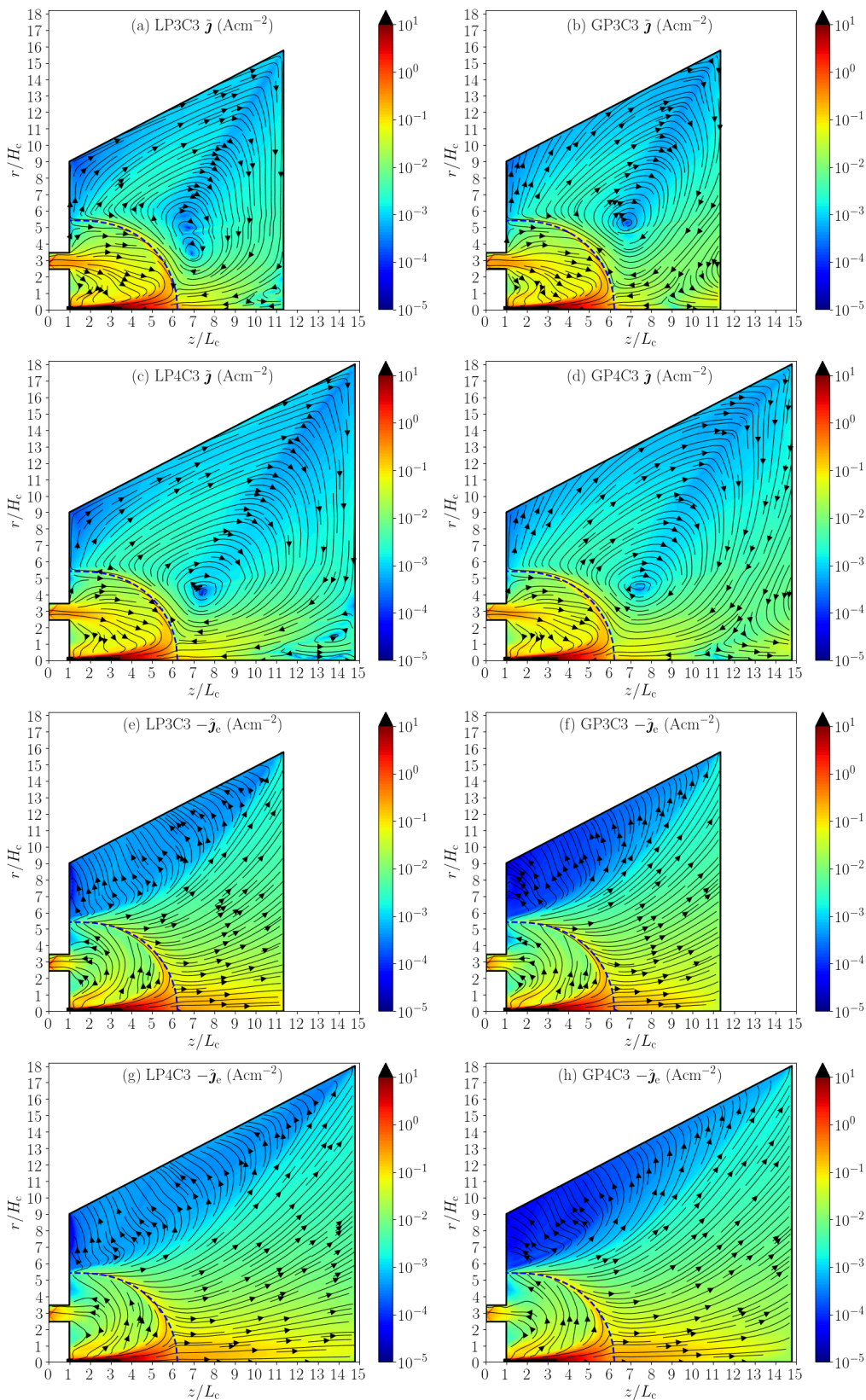


FIG. 7. Plume sizes P3 and P4 with C3 (black square marker) and with LPC (left column) and GPC (right column). 2D ( $z, r$ ) contour maps of  $\tilde{j}$  (a)-(d) and  $-\tilde{j}_e$  (e)-(h). The black lines with arrows depict streamlines of  $\tilde{j}$  and  $-\tilde{j}_e$ . The blue dashed lines correspond to the MS.

## 1 2 V. CONCLUSION

3  
4  
5  
6  
7  
8  
9  
10  
11  
12  
13  
14  
15  
16  
17  
18  
19 Three major aspects of the numerical modelling of the near plume of a HET have been investigated in this work through the hybrid code HYPHEN. First, regarding boundary conditions imposed at the plume boundary P, a new GPC model, which enforces a net current-free condition at P, has been developed to overcome the limitations of the widely adopted LPC model, that imposes zero plasma current locally, i.e., at every point along the plume boundary. Second, the influence of plume size on the plasma solution, particularly on the electric current maps, have been assessed for both the GPC and LPC models. And third, the effects of the cathode location on the discharge performance and the coupling between cathode electrons and the ion beam have been investigated for externally-mounted cathodes, located inside (C1) and outside (C2) of the MS, and for a centrally-mounted cathode (C3).

20  
21  
22  
23  
24  
25  
26  
27  
28  
29  
30  
31  
32 For C1, the results for four plume sizes indicate that the GPC model provides a more robust plasma current solution against plume truncation. Differences in the plasma current between cases are primarily due to changes on the electron current. The GPC is found to limit electron detachment from magnetic lines induced by the plume boundary, providing an electron current solution that is more representative of the still magnetized electron population in the near plume region. For a sufficiently large plume, changes on the coupling voltage with plume size are small relative to the discharge voltage. Therefore, the expansion of the ion beam and the thruster performance are minimally affected by the plume condition.

33  
34  
35  
36  
37  
38  
39  
40  
41  
42  
43 Compared to C1 cases, the discharge performance of C2 cases is poorer: thrust efficiency is 2-3% lower due to higher plume divergence and velocity dispersion. The cathode-beam coupling is weaker, and higher electric potential and electron temperature values are observed in the plume. The opposite behavior is found for C3: thrust efficiency is 2-3% higher than for C1 cases due to lower plume divergence and velocity dispersion. The cathode-beam coupling is improved and lower electric potential and electron temperature values are found in the plume. These results are consistent with previous experimental and numerical results in the literature.

44  
45  
46  
47  
48  
49  
50  
51  
52  
53 The plasma current solution provided by the LPC is directly dependent on the plume size for C2 cases, making it unreliable. In this scenario, the GPC clearly outperforms the LPC: by locally decoupling ion and electron currents at P, it eliminates the artificial effects present on the electric current solution obtained with the LPC, providing a significantly more robust solution for different plume sizes, and thus increasing the reliability of the simulation results obtained for smaller, less computationally demanding plume domains. This fact is of central importance for comparison of simulation results with experimental data, which are mostly obtained in the plume.

54  
55  
56  
57 Regardless of the plume condition, plume size, or cath-

58  
59  
60 ode location, no electron cooling is observed in the downstream MN-shaped region of the plume. The higher electron temperature observed in the plume for C2 cases increases the potential drop between P and infinity. These results highlight the need for a model to account for the experimentally observed cooling in HET plumes. Future efforts will concentrate on incorporating an anomalous electron cooling model, as the one proposed by Zhou *et al.* in Ref. 36, and on evaluating the new GPC model in scenarios representative of magnetically-shielded HETs with centrally-mounted cathodes, cylindrical HETs and electrodeless plasma thrusters with MN.

## DATA AVAILABILITY STATEMENT

The data that support the findings of this study are available from the corresponding author upon reasonable request.

## ACKNOWLEDGMENTS

This work has been supported by the CHEOPS LOW POWER project, funded by the European Union's Horizon 2020 Research and Innovation Program, under Grant Agreement number 101004331.

We thank Dr. Jesús Perales-Díaz for his active collaboration in the development of the numerical models and constructive comments.

## Appendix A: Power balance and thrust efficiency

The plasma power balance for the steady state discharge is

$$P = P_P + P_D + P_A + P_{\text{inel}}, \quad (\text{A.1})$$

where:  $P = I_d V_d + P_C$  is the total power deposited into the plasma discharge, which is the sum of the discharge power,  $P_d = I_d V_d$ , and the net power delivered through cathode electron emission,  $P_C$ , amounting to 1-2% of  $P$ ;  $P_P$  is the plasma energy flow through P boundary;  $P_D$  and  $P_A$  are the power losses at the dielectric walls and at the anode wall, respectively; and  $P_{\text{inel}}$  corresponds to the power losses due to inelastic (e.g., ionization and excitation) collisions. All powers are defined as positive. The value of  $P_{\text{inel}}$  is obtained from a volumetric integral;  $P_P$ , is computed from the surface integral at the downstream plume boundary P (the integral of  $P''_{niP}$  and  $P''_{neP}$  yields the contribution of ions and electrons, respectively); and the values of  $P_D$  and  $P_A$  come from surface integrals at the respective walls.

The thrust efficiency is defined and factorized as

$$\eta = \frac{F^2}{2\dot{m}P} \equiv \eta_{\text{ene}}\eta_{\text{div}}\eta_{\text{disp}}, \quad (\text{A.2})$$

where the energy, divergence, and dispersion efficiencies are defined, respectively, as

$$\eta_{\text{ene}} = \frac{P_P}{P}, \quad \eta_{\text{div}} = \frac{P_{zP}}{P_P}, \quad \eta_{\text{disp}} = \frac{F^2}{2\dot{m}P_{zP}}, \quad (\text{A.3})$$

with  $P_{zP}$  the flow of axial plasma energy across P. In Eq. (A.3),  $\eta_{\text{ene}}$  is a plasma source related efficiency that measures the relative power in the downstream plume, while plume-related efficiencies are  $\eta_{\text{div}}$ , which assesses the plume divergence based on axial energy and total energy flows, and  $\eta_{\text{disp}}$ , that quantifies the level of velocity dispersion of all plasma species (which would be one for a mono-velocity gas).

## REFERENCES

- <sup>1</sup>Tilley, D., de Grys, K., and Myers, R., "Hall thruster-cathode coupling," *35th Joint Propulsion Conference and Exhibit*, 1999, p. 2865.
- <sup>2</sup>Jameson, K. K., Goebel, D. M., Hofer, R. R., and Watkins, R. M., "Cathode coupling in Hall thrusters," *30<sup>th</sup> International Electric Propulsion Conference*, No. IEPC-2007-278, Electric Rocket Propulsion Society, Fairview Park, OH, Florence, Italy, September 17–20, 2007.
- <sup>3</sup>Beal, B. E., Gallimore, A. D., and Hargus Jr, W. A., "Effects of cathode configuration on Hall thruster cluster plume properties," *Journal of Propulsion and Power*, Vol. 23, No. 4, 2007, pp. 836–844.
- <sup>4</sup>Hofer, R., Johnson, L., Goebel, D., and Wirz, R., "Effects of internally mounted cathodes on Hall thruster plume properties," *IEEE Transactions on Plasma Science*, Vol. 36, No. 5, 2008, pp. 2004–2014.
- <sup>5</sup>McDonald, M. and Gallimore, A., "Cathode position and orientation effects on cathode coupling in a 6-kW Hall thruster," *31<sup>st</sup> International Electric Propulsion Conference*, No. IEPC-2009-113, Electric Rocket Propulsion Society, Fairview Park, OH, University of Michigan, Ann Arbor, MI, USA, September 20–24, 2009.
- <sup>6</sup>Sommerville, J. and King, L., "Effect of cathode position on Hall-effect thruster performance and near-field plume properties," *44th AIAA/ASME/SAE/ASEE Joint Propulsion Conference & Exhibit*, No. AIAA-2008-4996, American Institute of Aeronautics and Astronautics, Reston, VA, Hartford, CT, USA, July 21–23, 2007.
- <sup>7</sup>Sommerville, J. D. and King, L. B., "Hall-effect thruster–cathode coupling, part II: ion beam and near-field plume," *Journal of Propulsion and Power*, Vol. 27, No. 4, 2011, pp. 754–767.
- <sup>8</sup>Turan, N., Kokal, U., Celik, M., and Kurt, H., "Experimental study of the effects of the cathode position and the electrical circuit configuration on the operation of HK40 Hall thruster and BUSTLab hollow cathode," *52nd AIAA/SAE/ASEE Joint Propulsion Conference*, No. AIAA-2016-4834, American Institute of Aeronautics and Astronautics, Reston, VA, Salt Lake City, UT, USA, July 25–27, 2016.
- <sup>9</sup>Yu, D., Meng, T., Ning, Z., and Liu, H., "Confinement effect of cylindrical-separatrix-type magnetic field on the plume of magnetic focusing type Hall thruster," *Plasma Sources Science and Technology*, Vol. 26, No. 4, 2017, pp. 04LT02.
- <sup>10</sup>Ding, Y., Li, H., Li, P., Jia, B., Wei, L., Su, H., Sun, H., Wang, L., and Yu, D., "Effect of relative position between cathode and magnetic separatrix on the discharge characteristic of Hall thrusters," *Vacuum*, Vol. 154, 2018, pp. 167–173.
- <sup>11</sup>Frieman, J. D., King, S. T., Walker, M. L., Khayms, V., and King, D., "Role of a conducting vacuum chamber in the Hall effect thruster electrical circuit," *Journal of Propulsion and Power*, Vol. 30, No. 6, 2014, pp. 1471–1479.
- <sup>12</sup>Frieman, J. D., Walker, J. A., Walker, M. L., Khayms, V., and King, D. Q., "Electrical facility effects on Hall thruster cathode coupling: Performance and plume properties," *Journal of Propulsion and Power*, Vol. 32, No. 1, 2016, pp. 251–264.
- <sup>13</sup>Walker, J. A., Frieman, J. D., Walker, M. L., Khayms, V., King, D., and Peterson, P. Y., "Electrical facility effects on Hall-effect-thruster cathode coupling: discharge oscillations and facility coupling," *Journal of Propulsion and Power*, Vol. 32, No. 4, 2016, pp. 844–855.
- <sup>14</sup>Walker, J. A., Langendorf, S. J., Walker, M. L., Khayms, V., King, D., and Pertson, P., "Electrical facility effects on Hall current thrusters: electron termination pathway manipulation," *Journal of Propulsion and Power*, Vol. 32, No. 6, 2016, pp. 1365–1377.
- <sup>15</sup>Fife, J. M., *Hybrid-PIC modeling and electrostatic probe survey of Hall thrusters*, Ph.D. thesis, Massachusetts Institute of Technology, 1998.
- <sup>16</sup>Hagelaar, G., Bareilles, J., Garrigues, L., and Boeuf, J., "Two-dimensional model of a stationary plasma thruster," *Journal of Applied Physics*, Vol. 91, No. 9, 2002, pp. 5592–5598.
- <sup>17</sup>Parra, F. I., Ahedo, E., Fife, J. M., and Martínez-Sánchez, M., "A two-dimensional hybrid model of the Hall thruster discharge," *Journal of Applied Physics*, Vol. 100, No. 2, 2006, pp. 023304.
- <sup>18</sup>Garrigues, L., Hagelaar, G., Boniface, C., and Boeuf, J., "Anomalous conductivity and secondary electron emission in Hall effect thrusters," *Journal of applied physics*, Vol. 100, No. 12, 2006, pp. 123301.
- <sup>19</sup>Sommier, E., Scharfe, M., Gascon, N., Cappelli, M., and Fernandez, E., "Simulating plasma-induced Hall thruster wall erosion with a two-dimensional hybrid model," *Plasma Science, IEEE Transactions on*, Vol. 35, No. 5, 2007, pp. 1379–1387.
- <sup>20</sup>Perales-Díaz, J., Domínguez-Vázquez, A., Fajardo, P., Ahedo, E., Faraji, F., Reza, M., and Andreussi, T., "Hybrid plasma simulations of a magnetically shielded Hall thruster," *Journal of Applied Physics*, Vol. 131, No. 10, 2022, pp. 103302.
- <sup>21</sup>Cichocki, F., Domínguez-Vázquez, A., Merino, M., Fajardo, P., and Ahedo, E., "Three-dimensional neutralizer effects on a Hall-effect thruster near plume," *Acta Astronautica*, Vol. 187, 2021, pp. 498–510.
- <sup>22</sup>Mikellides, I. and Katz, I., "Numerical simulations of Hall-effect plasma accelerators on a magnetic-field-aligned mesh," *Physical Review E*, Vol. 86, No. 4, 2012, pp. 046703.
- <sup>23</sup>Keidar, M., Boyd, I. D., and Beilis, I. I., "Modeling of a high-power thruster with anode layer," *Physics of Plasmas*, Vol. 11, No. 4, 2004, pp. 1715–1722.
- <sup>24</sup>Andreussi, T., Giannetti, V., Leporini, A., Saravia, M. M., and Andrenucci, M., "Influence of the magnetic field configuration on the plasma flow in Hall thrusters," *Plasma Phys. Control. Fusion*, Vol. 60, No. 1, 2018.
- <sup>25</sup>Lopez Ortega, A. and Mikellides, I. G., "The importance of the cathode plume and its interactions with the ion beam in numerical simulations of Hall thrusters," *Physics of Plasmas*, Vol. 23, No. 4, 2016, pp. 043515.
- <sup>26</sup>Mikellides, I. G., Katz, I., Hofer, R. R., and Goebel, D. M., "Hall-effect thruster simulations with 2-D electron transport and hydrodynamic ions," *31<sup>st</sup> International Electric Propulsion Conference*, paper 2009-114, Electric Rocket Propulsion Society, Fairview Park, OH, University of Michigan, Ann Arbor, MI, USA, 2009.
- <sup>27</sup>Kubota, K., Cho, S., Watanabe, H., and Funaki, I., "Hybrid-PIC Simulation of Hall Thruster with Internally Mounted Cathode," *35<sup>th</sup> International Electric Propulsion Conference*, IEPC-2017-426, Atlanta, GA, USA, 2017.
- <sup>28</sup>Cho, S., Kubota, K., Watanabe, H., Hara, K., and Funaki, I., "Comparing Internal and External Cathode Boundary Position in a Hall Thruster Particle Simulation," *35<sup>th</sup> International Electric Propulsion Conference*, No. IEPC-2017-402, Electric Rocket Propulsion Society, Fairview Park, OH, Georgia Institute of

- Technology, Atlanta, GA, USA, October 8-12, 2017.
- <sup>29</sup>Cao, X., Liu, H., and Yu, D., "Simulation of discharge process of Hall thruster under the internal and external cathode conditions," *The European Physical Journal Applied Physics*, Vol. 90, No. 1, 2020, pp. 10801.
- <sup>30</sup>Domínguez-Vázquez, A., *Axisymmetric simulation codes for Hall effect thrusters and plasma plumes*, Ph.D. thesis, Universidad Carlos III de Madrid, Leganés, Spain, 2019.
- <sup>31</sup>Domínguez-Vázquez, A., Zhou, J., Fajardo, P., and Ahedo, E., "Analysis of the plasma discharge in a Hall thruster via a hybrid 2D code," *36<sup>th</sup> International Electric Propulsion Conference*, No. IEPC-2019-579, Electric Rocket Propulsion Society, Vienna, Austria, 2019.
- <sup>32</sup>Duchemin, O., Rabin, J., Balika, L., Coduti, G., Vial, V., Vuglec, D., Cavelan, X., and Leroi, V., "Qualification Status of the PPS-5000 Hall Thruster Unit," *36<sup>th</sup> International Electric Propulsion Conference*, No. IEPC-2019-906, Electric Rocket Propulsion Society, Fairview Park, OH, 2019.
- <sup>33</sup>Duchemin, O. B., Rabin, J., Coduti, G., and Le Méhauté, D., "Expanding the Mission Capture of the PPS® 5000 Hall Thruster," *ASCEND 2023*, 2023, p. 4790.
- <sup>34</sup>Ahedo, E. and Merino, M., "Two-Dimensional Supersonic Plasma Acceleration in a Magnetic Nozzle," *Physics of Plasmas*, Vol. 17, No. 7, 2010, pp. 073501.
- <sup>35</sup>Zhou, J., *Modeling and simulation of the plasma discharge in a radiofrequency thruster*, Ph.D. thesis, Universidad Carlos III de Madrid, Leganés, Spain, 2021.
- <sup>36</sup>Zhou, J., Domínguez-Vázquez, A., Fajardo, P., and Ahedo, E., "Magnetized fluid electron model within a two-dimensional hybrid simulation code for electrodeless plasma thrusters," *Plasma Sources Science and Technology*, Vol. 31, No. 4, 2022, pp. 045021.
- <sup>37</sup>Pérez-Grande, D., González-Martínez, O., Fajardo, P., and Ahedo, E., "Analysis of the numerical diffusion in anisotropic mediums: benchmarks for magnetic field aligned meshes in space propulsion simulations," *Applied Sciences*, Vol. 6, No. 11, 2016, pp. 354.
- <sup>38</sup>Ahedo, E. and Pablo, V., "Combined effects of electron partial thermalization and secondary emission in Hall thruster discharges," *Physics of Plasmas*, Vol. 14, 2007, pp. 083501.
- <sup>39</sup>Lam, C. M., Fernandez, E., and Cappelli, M. A., "A 2-D hybrid Hall thruster simulation that resolves the ExB electron drift direction," *IEEE Transactions on Plasma Science*, Vol. 43, 2015, pp. 86–94.
- <sup>40</sup>Marks, T. A., Mikellides, I. G., Lopez Ortega, A., and Jorns, B., "Hall2De Simulations of a Magnetic Nozzle," *AIAA Propulsion and Energy 2020 Forum*, AIAA 2020-3642, 2020.
- <sup>41</sup>Merino, M. and Ahedo, E., "Plasma detachment in a propulsive magnetic nozzle via ion demagnetization," *Plasma Sources Science and Technology*, Vol. 23, No. 3, 2014, pp. 032001.
- <sup>42</sup>Jorns, B. A. and Byrne, M. P., "Model for the dependence of cathode voltage in a Hall thruster on facility pressure," *Plasma Sources Science and Technology*, Vol. 30, No. 1, 2021, pp. 18.
- <sup>43</sup>Ahedo, E., Correyero, S., Navarro, J., and Merino, M., "Macroscopic and parametric study of a kinetic plasma expansion in a paraxial magnetic nozzle," *Plasma Sources Science and Technology*, Vol. 29, No. 4, 2020, pp. 045017.
- <sup>44</sup>Zhou, J., Sánchez-Arriaga, G., and Ahedo, E., "Time-dependent expansion of a weakly-collisional plasma beam in a paraxial magnetic nozzle," *Plasma Sources Science and Technology*, Vol. 30, No. 4, 2021, pp. 045009.